Magnitude-order improvements to the measurement precision of Antarctic grounding zone dynamics using SAR satellite constellations

Evan L. Kramer and Brent M. Minchew

Division of Geological and Planetary Sciences,
California Institute of Technology, Pasadena, CA 91125, USA

Corresponding author: Evan L. Kramer (elkramer@caltech.edu)
Brent M. Minchew (minchew@caltech.edu)

Preprint statement

This is a non-peer-reviewed preprint submitted to **EarthArXiv**. This manuscript has been submitted to *IEEE Geoscience and Remote Sensing Letters* for peer review. As a non-peer-reviewed preprint, subsequent versions of this manuscript may have differing content.

Magnitude-order improvements to the measurement precision of Antarctic grounding zone dynamics using SAR satellite constellations

Evan L. Kramer, and Brent M. Minchew,

Abstract—**Glacier loss in Antarctica is strongly influenced by melt in the grounding zone, the transition between grounded and floating ice. Thwaites Glacier is a critical region, with 65 cm of sea-level-equivalent ice. A recent dataset tracks grounding line retreat for Thwaites and other Antarctic ice streams over 30 years. Despite this long-term record, significant uncertainty remains in predictions of ice sheet stability. An important source and diagnostic of this uncertainty is the poorly constrained response of grounding zones to high-frequency tidal forcing, driven by a lack of observations at the temporal resolution needed to capture short-timescale viscoelastic ice flexure. Commercial SAR constellations offer an opportunity to close this gap. We demonstrate this by identifying on-orbit InSAR-capable commercial SAR satellites suitable for ice shelf monitoring and propagating their orbits over four tidal beat cycles for the dominant constituents near Thwaites. The Cramér-Rao lower bounds on secular ice velocity and vertical tidal displacement reveal a two to three-fold improvement in measurement precision for an observation campaign using current commercial SAR satellites compared to the NISAR satellite. Further analysis shows that three orders of magnitude improvement in measurement precision can be achieved through the cross-satellite multi-plane TWIST InSAR architecture that enables sub-daily temporal baselines and breaks the K1 tidal aliasing barrier of one-day repeat sampling. Full inversions of synthetic surface displacement confirm the complete recovery of composite tidal forcing signals. The results offer a practical pathway for acquiring consistent observations that improve understanding of ice dynamics and projections of sea level rise.**

Index Terms—**Grounding zone, Tidal forcing, SAR observations, TWIST InSAR**

I. Introduction and Background

Ice shelves lining the coast of Antarctica exert a primary control on the stability of the continent's grounded ice sheets by providing buttressing stresses that resist the seaward flow of ice and largely control the position of the grounding line, where the ice sheet goes afloat [1], [2]. Buttressing is facilitated by shear along the lateral margins, pinning points where the ice contacts bathymetric highs, and hydrostatic pressure at the calving front. These stresses are transmitted across grounding lines and can influence the speed of glacier flow for tens to hundreds of kilometers inland over timescales from days to decades [3], [4], [5]. Grounding lines are known to migrate up to several kilometers as a function of the local tidal forcing, which can influence the hydrology and sub-ice shelf melt rates in the broader grounding zone [6], [7]. Melt and other processes occurring in the broader grounding zone are important to characterize because ocean-driven melting affects grounding line persistence on highs in bed topography and has a strong influence on glacier retreat and sea level projections [8], [9].

E. Kramer and B. Minchew are with the Division of Geological and Planetary Sciences, California Institute of Technology, Pasadena, CA, 91125 USA e-mail: elkramer@caltech.edu

It follows that accurately locating grounding lines and measuring the broader dynamics of the grounding zone is necessary to understand how the West Antarctic Ice Sheet evolves and contributes to sea level rise. Grounding line locations can be inferred by observing the dynamical response of the system to a known forcing. The flexure zone is the area where tidal forcing drives cyclic bending of the ice shelf and modulates ice velocity, strain, and basal contact conditions on short timescales. Compared to the spatial scale of grounding line migration, the flexure zone can span an order of magnitude larger spatial scale at tens of kilometers. Measurements of the vertical motion of the ice shelf within the flexure zone in response to tidal forcing can be used to infer ice flow velocity, strain rates, and the background stress field. These estimates, in turn, provide constraints on grounding line position.

A common observing system for consistent surface vertical displacement measurements across large areas is space-based synthetic aperture radar (SAR). SAR satellites that precisely maintain their orbital configuration offer interferometric (InSAR) measurement capabilities when a pair of observations is acquired at different times from the same relative satellite-target position. InSAR utilizes differences between the electromagnetic phase of the two SAR observations to quantify displacements in the line of sight direction of the sensor with a resolution set to a fraction of the sensor's operating wavelength. When two InSAR measurements are differenced, they form a differential InSAR (DInSAR) product, a standard approach in ice sheet remote sensing that removes the steady horizontal component of ice flow and isolates the vertical displacement driven by tidal forcing. This technique underpins continental-scale grounding line datasets, such as [10], which synthesizes more than 30 years of DInSAR observations from a virtual constellation of SAR satellites operated by multiple national space agencies and commercial providers. The result is the most complete time history of Antarctic grounding line migration to date. While this dataset captures the long term behavior of grounding line retreat over 30 years, it does not address any aspect related to the transient response of the system to short term forcings that influence long term grounding zone trends.

The characteristics of the local tidal forcing dictate the frequency and timescale over which observations must occur to capture a complete understanding of transient dynamics. Of particular interest is the ability to eliminate aliasing in the inversion of the absolute response to a superposition of individual tidal constituents and to resolve the relative response to the individual tidal constituents over the harmonic beat period. Observation campaigns designed to address both aspects will provide valuable insights into grounding zone dynamics and processes. A critical limitation of the current dataset is its one-day minimum InSAR temporal baseline, or the time between a pair of interferable SAR observations. While sufficient for detecting long-term geometric changes in grounding line position, this sampling interval is too coarse to resolve the short-period processes that govern ice deformation within the flexure zone. SAR observations with daily revisits were used to estimate grounding line locations for Thwaites Glacier, which is a significant contributor to sea level rise with an ice volume equivalent of 0.65 m of global sea level [7]. The dominant tidal forcing in the region occurs at diurnal and semidiurnal frequencies requiring InSAR observations with sub-daily temporal baselines to satisfy the Nyquist sampling criterion. While slight differences between tidal and daily observation frequencies permit reconstruction of the system response, not only is consistent sampling required for many forcing periods, but one must also contend with the superposition of other system changes with the signal of interest.

In the recently published grounding line dataset [10], the SAR satellites offering one-day temporal baselines are the COSMO-SkyMed and ICEYE constellations, both of which operate at X-band radar frequencies. In terms of accessibility, COSMO-SkyMed data is restricted and requires formal project proposals to be submitted and approved through the European Space Agency or other national authorities. Commercial SAR constellations, such as ICEYE, Capella Space, and Umbra Space, operate as a user-driven, on-demand tasking service with streamlined procurement processes. While the preceding 30 years of DInSAR grounding line histories were defined by disjointed observations with minimum InSAR temporal baselines of one-day, the rapid expansion of the commercial SAR sector and the on-demand nature of its tasking model now make a fundamentally different observation strategy possible.

Here, we put forth a vision for the next 30 years that involves dedicated campaigns of dense time series InSAR observations with daily and sub-daily temporal baselines that are feasible with current on-orbit satellites and future constellation configurations respectively. Carefully designed acquisition campaigns leveraging existing commercial SAR satellites in repeat ground track (RGT) orbits yield two to three-fold improvements in the measurement precision of flexure zone dynamics over the current state of the art. We further show that the Tunable WIndow for Surface Transients (TWIST) InSAR architecture, a cross-satellite multi-plane constellation design detailed in [11], breaks the K1 tidal aliasing barrier through sub-daily temporal baselines and delivers a three orders of magnitude improvement in tidal measurement precision. Together, these capabilities open the door to directly observing the viscoelastic response and other dynamics of grounding zones to tidal forcing, enabling new constraints on ice–ocean coupling processes and informing the development of next-generation ice dynamics models used to project sea level rise.

II. Methodology

A. Study Area Definition

Thwaites Glacier was selected as the study area due to the significant societal implications that will arise from its increased instability and contribution to sea level rise. To define the study region, Antarctic coastlines and grounding line geometries were extracted using the MATLAB Antarctic Mapping Tools add-on in combination with the MEaSUREs Antarctic Boundaries product [12], [13], [14]. A closed polygon delineating the region of interest was constructed by taking the union of the seaward ice shelf boundary and the Thwaites grounding line, with a 50 km landward buffer applied to the grounded ice sheet. This procedure yielded a contiguous area of interest spanning approximately 19,000 km^2 and was intended to capture the full spatial extent over which tidal-induced strain propagates through the grounded portion of the ice sheet adjacent to the flexure zone.

To facilitate satellite observation modeling, the area of interest was subdivided into a grid of rectangular tiles measuring 30 km by 50 km, corresponding to the standard footprint of commercial SAR stripmap imaging products [15], [16]. The centroid of each tile was used as a representative target location for evaluating satellite line of sight access opportunities and interferometric observation feasibility. These centroid locations therefore serve as anchor points for the observation geometry analyses presented in the results section. To characterize the tidal forcing acting on the flexure zone in the vicinity of Thwaites Glacier, the CATS2008 model was used to identify the dominant tidal constituents and determine their associated amplitudes and frequencies [17]. The resulting tidal parameters were then used to compute the beat frequency between the dominant modes, which defines the minimum observation duration required to fully resolve the composite tidal signal in the measured ice displacement time series.

B. Orbit Modeling

Four SAR satellite observing systems are considered in this study: NISAR, a theoretical satellite with orbit parameters tuned for observing Thwaites Glacier, three currently on-orbit ICEYE satellites, and a theoretical TWIST InSAR constellation. All four SAR satellite observing systems are InSAR-capable and operate in repeat ground track (RGT) orbits to maintain phase coherence across multiple observations acquired from the same target-satellite relative geometry. RGT orbits repetitively trace the same projected curve on the Earth's surface by completing an integer number of satellite nodal periods over an integer number of nodal days [18]. While the NISAR and ICEYE satellite orbits are already defined, the RGT orbits for the theoretical tuned and TWIST InSAR satellites are designed in this work for the purposes of comparing observing system measurement precision. To design these orbits, a formulation which determines the orbit semi-major axis after specification of orbit inclination, eccentricity, right ascension of the ascending node (RAAN), and a similitude parameter defining the repeat cycle is adopted [19]. Inclination angle and RAAN were treated as free design variables and only circular orbits were considered when designing the theoretical tuned orbit. The similitude parameter was fixed to one nodal day divided by fifteen satellite revolutions, producing a one-day RGT configuration consistent with the RGT orbits employed by three currently on-orbit ICEYE SAR satellites.

In addition to influencing the design of the theoretical tuned orbit, the orbits of the three currently on-orbit one-day RGT ICEYE satellites were used as templates for designing the theoretical TWIST InSAR constellation. The TWIST InSAR mission architecture enables InSAR measurements at sub-daily temporal baselines through satisfaction of two conditions [11]. The first condition involves orientation of a phased satellite's orbit plane relative to a reference satellite's according to a desired temporal baseline. The second condition involves phasing the satellite's inter-plane position to ensure identical target-satellite relative geometries. In this work, a single TWIST InSAR pair was created by adding an additional satellite to the on-orbit ICEYE three satellite constellation. A sub-daily temporal baseline of six hours was defined. Additional TWIST InSAR pairs with other sub-daily temporal baselines were added to the existing three satellite constellation in a similar fashion for analyses of measurement performance as a function of constellation size. The TWIST InSAR constellation results were contrasted with the performance achieved by comparably-sized, but unphased InSAR constellations with RAAN offsets according to $\frac{360^\circ}{n_{\text{add}}+1}$ where n_{add} is the number of satellites added to the existing constellation.

The aforementioned ICEYE one-day RGT satellites, and more recently, Capella's three and seven-day RGT satellites have demonstrated InSAR capabilities. However, most commercial SAR satellites have orbital maintenance strategies that differ from those of traditional government-operated SAR missions. Publicly-funded institutionally-backed missions typically maintain tight control of orbit parameters to preserve long-term repeat geometry [20], [21], [22], [23], [24], [25]. Identification of ICEYE's three one-day RGT satellites was conducted by developing a status classification algorithm to analyze satellite state histories derived from publicly available two-line element (TLE) datasets maintained by the North American Aerospace Defense Command [26]. The classification algorithm modifies previous filtering approaches to identify the operational status of satellites by analyzing temporal variations in orbit parameters [27], [28]. Filtering parameters were tuned to account for the limited precision inherent in publicly distributed TLE state information. The resulting algorithm was applied to TLE data spanning February 10–17, 2026 to identify commercial SAR satellites that maintained stable orbit altitudes over a seven-day interval. Satellites meeting this criterion were analyzed to determine whether their orbit elements corresponded to RGT orbits.

For all SAR observing systems, orbit propagation was performed assuming Keplerian motion under central-body gravitational acceleration, neglecting perturbing forces in order to isolate the purely geometric aspects of observation opportunities. line of sight access conditions for SAR imaging were defined using incidence and squint angle limits from the literature. For commercial SAR satellites, incidence angle limits of 5°–45° and squint angles of $\pm 35^\circ$ were defined with both left and right looking capabilities. For the NISAR mission, incidence angle limits of 33°-47° and squint angles of $\pm 3^\circ$ were defined with a fixed left-looking configuration.

C. Measurement Performance

The ability of a satellite observing system to constrain geophysical parameters from interferometric measurements depends strongly on the geometry of the available observations and their timing relative to the forcing function. To quantify uncertainties in geophysical parameter estimation, we adopt a linear inverse formulation developed in previous works [3], [29], [30], [31] and cast its results in terms of the Fisher information matrix and the Cramér-Rao lower bound (CRLB), which together provide an intuitive framework for interpreting the fundamental limits on measurement precision imposed by orbit geometry and observation timing.

For a linear observation model of the form $\mathbf{d} = \mathbf{G}\mathbf{m} + \boldsymbol{\varepsilon}$, where $\boldsymbol{\varepsilon} \sim N(\mathbf{0}, \mathbf{C}_d)$, the Fisher information matrix is $\mathbf{F} = \mathbf{G}^T \mathbf{C}_d^{-1} \mathbf{G}$, and the CRLB states that the covariance of any unbiased estimator of $\mathbf{m}$ satisfies $\mathbf{Cov}(\hat{\mathbf{m}}) \geq \mathbf{F}^{-1}$. Setting $\mathbf{C}_d = \mathbf{I}$ isolates the contribution of orbit geometry and observation timing, yielding $\mathbf{F} = \mathbf{G}^T\mathbf{G}$ and $\mathbf{Cov}(\hat{\mathbf{m}}) \geq (\mathbf{G}^T\mathbf{G})^{-1}$. Two formulations of the design matrix are considered. For the purely geometric case, the design matrix $\mathbf{H}$ has rows consisting of the unit line of sight vectors pointing from each target location toward the satellite for each interferometric observation as shown in equation 1.

$$\mathbf{H} = \begin{bmatrix} l_{x,1}\Delta t_1 & l_{y,1}\Delta t_1 & l_{z,1}\Delta t_1 \\ \vdots & \vdots & \vdots \\ l_{x,n}\Delta t_n & l_{y,n}\Delta t_n & l_{z,n}\Delta t_n \end{bmatrix} \tag{1}$$

The CRLB on three-dimensional ice velocity estimation is then $\mathbf{C}_{\text{geo}} = (\mathbf{H}^T\mathbf{H})^{-1}$, and the geometric measurement precision metrics are given in equation 2.

$$\begin{aligned} \sigma_{\text{geo,total}} &= \sqrt{\text{tr}(\mathbf{C}_{\text{geo}})} \\ \sigma_{\text{geo,hor}} &= \sqrt{C_{\text{geo}}(1,1) + C_{\text{geo}}(2,2)} \\ \sigma_{\text{geo,ver}} &= \left(\sum_{i=1}^{n} l_{z,i}^2\right)^{-1/2} \end{aligned} \tag{2}$$

For the tidal formulation, the design matrix $\mathbf{G}$ incorporates the periodic temporal structure of tidal deformation by multiplying the vertical line of sight component by harmonic basis functions for the K_1 and O_1 diurnal constituents as shown in equation 3.

$$\mathbf{G} = \left[\begin{matrix} l_{z,1}\Delta c(\omega_{K1}, t_{m,1}, t_{s,1}) & l_{z,1}\Delta s(\omega_{K1}, t_{m,1}, t_{s,1}) \\ \vdots & \vdots \\ l_{z,n}\Delta c(\omega_{K1}, t_{m,n}, t_{s,n}) & l_{z,n}\Delta s(\omega_{K1}, t_{m,n}, t_{s,n}) \\ l_{z,1}\Delta c(\omega_{O1}, t_{m,1}, t_{s,1}) & l_{z,1}\Delta s(\omega_{O1}, t_{m,1}, t_{s,1}) \\ \vdots & \vdots \\ l_{z,n}\Delta c(\omega_{O1}, t_{m,n}, t_{s,n}) & l_{z,n}\Delta s(\omega_{O1}, t_{m,n}, t_{s,n}) \end{matrix} \right] \tag{3}$$

The resulting CRLB, $\mathbf{C}_{\text{tid}} = (\mathbf{G}^T\mathbf{G})^{-1}$, bounds the precision of tidal constituent estimation, and the associated scalar metrics are given in equation 4.

$$\begin{aligned}\sigma_{\text{tid,total}} &= \sqrt{\text{tr}(\mathbf{C}_{\text{tid}})} \\ \sigma_{\text{tid,K1}} &= \sqrt{C_{\text{tid}}(1,1) + C_{\text{tid}}(2,2)} \\ \sigma_{\text{tid,O1}} &= \sqrt{C_{\text{tid}}(3,3) + C_{\text{tid}}(4,4)}\end{aligned} \tag{4}$$

These metrics are the square roots of the diagonal CRLB entries and represent lower bounds on the standard deviation of the corresponding parameter estimates relative to unit observation noise. Smaller values of σ_{geo} and σ_{tid} therefore indicate improved measurement precision, with the geometric and tidal components separately quantifying the observing system's ability to resolve three-dimensional ice motion and the dominant tidal forcing signals respectively. Previous works implemented similar linear inverse formulations and used measurement precision metrics position and tidal dilution of precision, PDOP and TDOP, which are equivalent to σ_{geo} and σ_{tid} in the current formulation [3], [29], [30], [31]. Contributions to uncertainty from the data covariance matrix, such as atmospheric phase delay or instrument noise, are not included, allowing the analysis to focus on the limits imposed by satellite orbit configurations and observation timing.

The CRLB analyses described above isolate the geometric and temporal contributions to measurement precision and provide a useful basis for comparing observing system designs. To complement these analyses and produce the surface displacement reconstructions shown in figure 6, a full inversion was performed for both secular ice motion and the vertical tidal displacement amplitudes using the formulation described in [3]. The combined design matrix, $\mathbf{A}$, concatenates a secular block, in which each row contains the unit line of sight components (l_E, l_N, l_U) scaled by the interferometric temporal baseline $\Delta t = t_m - t_s$, with a tidal block, in which each row contains the vertical line of sight component l_U multiplied by the differenced harmonic basis functions $\cos(\omega_p t_m) - \cos(\omega_p t_s)$ and $\sin(\omega_p t_m) - \sin(\omega_p t_s)$ for each tidal constituent $p \in \{K1, O1\}$. The model parameter vector is therefore $m = [v_E, v_N, v_U, a_{K1}, b_{K1}, a_{O1}, b_{O1}]^T$ where (v_E, v_N, v_U) are secular ice velocity components and (a_p, b_p) are the cosine and sine coefficients of the vertical tidal displacement for constituent p. Unlike the CRLB calculations in which $\mathbf{C}_d = \mathbf{I}$, the inversion in figure 6 employs a diagonal data covariance matrix whose inverse $\mathbf{V} = \mathbf{C}_d^{-1}$ has entries $V_{ii} = 2N_L\gamma_i^2/(1-\gamma_i^2)$, the standard Cramer-Rao expression for the inverse variance of interferometric phase, where N_L is the number of looks and γ_i is the interferometric coherence of the ith observation. Coherence values are assigned independently to each observation by drawing from a Gaussian distribution with mean 0.8 and standard deviation 0.1, capped below unity to avoid singularities. The estimate $\hat{\mathbf{m}}$ is obtained by solving the regularized weighted normal equations

$$\left(\mathbf{A}^T\mathbf{V}\mathbf{A}\right)\hat{\mathbf{m}} = \mathbf{A}^T\mathbf{V}\mathbf{d} \tag{5}$$

where $\mathbf{d}$ is the vector of synthetic line of sight displacements generated from the prescribed background velocity field and the composite K1 + O1 tidal forcing. The system is solved using a QR-based least-squares routine with column pivoting.

III. Results

The top row of figure 1 serves as a roadmap for the proceeding results and discussion. While the analyses presented in this paper focus on the fast moving Thwaites Glacier in West Antarctica, many other ice streams are also quickly flowing into the ocean [13]. Ice that moves past the grounding line at these outlets locally mixes with warm sea water. The ice speed and ocean temperature data establish long term trends, but they do not provide insight into the underlying transient processes at play. As discussed in the introduction, the current state of the art in space-based InSAR surface displacement measurements have temporal baselines of one day. Current systems offer coverage of Thwaites, annotated by the red box, and near-total spatial coverage of the entire Antarctic continent. These satellites operate in different orbital planes and therefore observe Thwaites, and other targets, from different observation geometries. This work shows that insights into the underlying transient processes at play in grounding zones can begin to be elucidated by robust data collection campaigns using existing on-orbit satellites. Further substantial improvement in observation capabilities and the ensuing characterization of transient grounding zone processes is demonstrated through implementation of a TWIST InSAR configuration offering sub-daily temporal baselines with near-identical spatial coverage. The middle row of figure 1 shows the tidal amplitude decomposition for Thwaites Glacier. Diurnal constituents represent a substantial fraction of the total tidal signal in the region, meaning that the observed displacement of the ice shelf reflects a composite response to multiple closely spaced tidal frequencies. Resolving the contributions of individual constituents therefore requires observations that both sample the tidal cycle frequently and span the beat period between dominant modes. The bottom row of figure 1 illustrates the superposition of the dominant diurnal tidal constituents K1 and O1 in the Thwaites Glacier region over 3.5 beat cycles. This tidal signal is displayed with the temporal baselines of SAR satellites used to construct the recent continent-wide DInSAR grounding line dataset, illustrating that most historical acquisitions occur at intervals longer than the periods of dominant tidal constituents.

Among the sensors represented in that dataset, only the constellations with one-day repeat capabilities, such as ICEYE and COSMO-SkyMed, provide temporal baselines dense enough to begin resolving individual tidal contributions to observed surface displacement, as previously demonstrated [3]. All interferometric-capable satellites in these constellations operate in one-day repeat orbits resulting in minimum temporal baselines of one nodal day between interferable observations in the dataset. Sampling daily is problematic because it aliases the K1 (23.93-hour period), S2 (12-hour period), and P1 (24.07-hour period) tidal constituents. As a result, diurnal tidal variability becomes folded into lower-frequency signals in the displacement time series, obscuring the true flexure in the grounding zone. Interferometric pairs

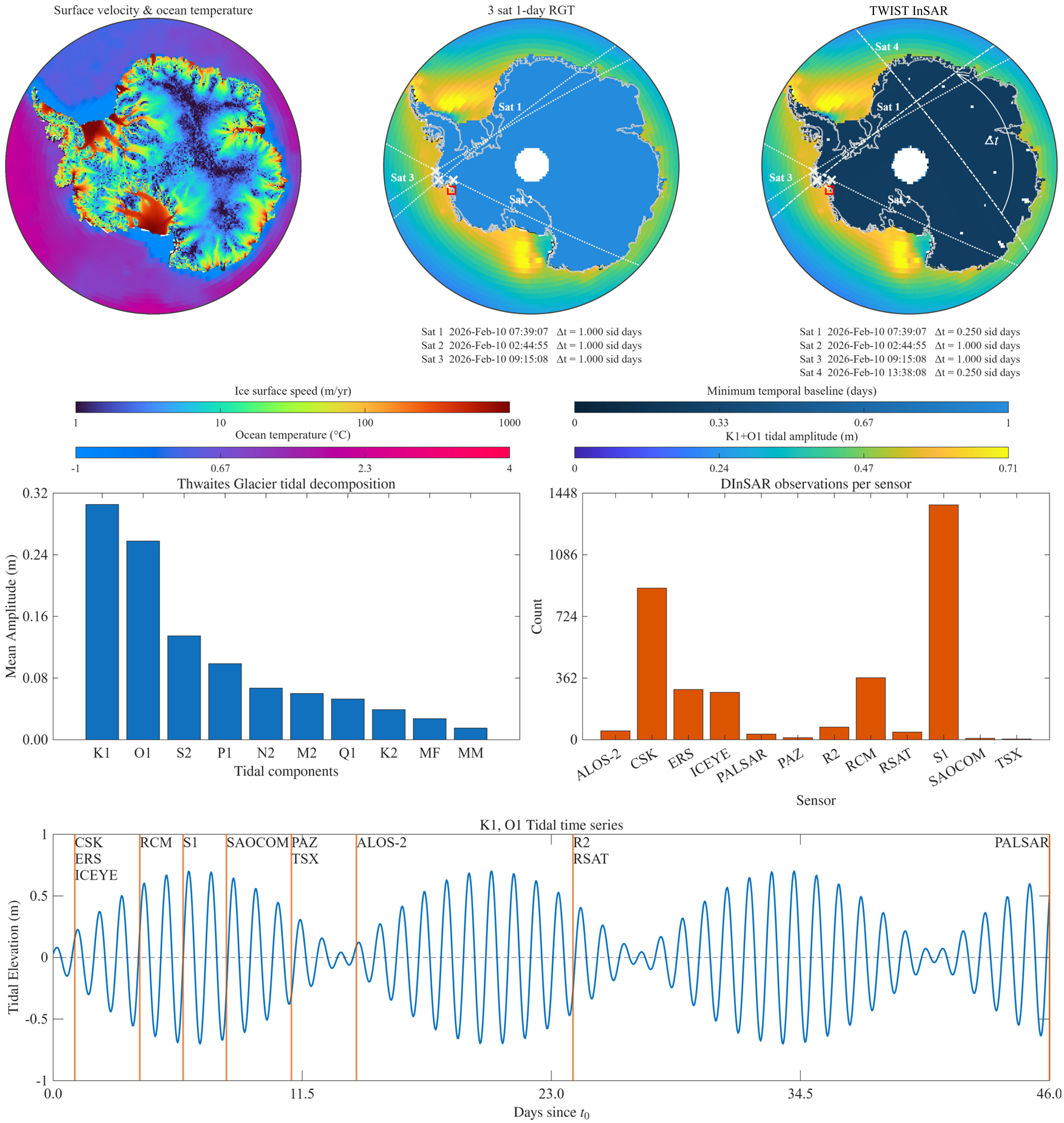

Fig. 1. Top row: Three maps of Antarctica establishing the context for the need to observe grounding zones (left), the current state of the art in InSAR temporal baseline (middle), and the achievable InSAR temporal baseline for future systems (right). Middle row: Decomposition of tidal constituents in the Amundsen Sea around Thwaites Glacier (left) and sensor distribution of DInSAR observations in the current state of the art grounding line dataset [10] (right). Bottom row: Tidal time series of the dominant K1 and O1 constituents over approximately 3.5 beat frequencies. Vertical lines show the temporal baseline for different satellites whose first SAR image was collected at $t = 0$.

with sub-daily temporal baselines would break this degeneracy by sampling multiple phases of the tidal cycle within a day.

A single satellite does not have the capacity to acquire interferometric observation pairs with sub-daily temporal baselines. However, a constellation of satellites operating in one-day repeat orbits can provide a high density set of interferometric observation pairs over the course of a day that could enable disentanglement of high frequency tidal signatures. To quantify the density of interferometric observations, each with one-day temporal baselines, that can be acquired, the number of observation opportunities of Thwaites Glacier as a function of RGT orbit altitude was analyzed. Figure 2 shows the number of observation opportunities available when restricting the search to repeat intervals between one and four nodal days and orbit altitudes below 1500 km, consistent with typical low Earth orbit (LEO) operations for commercial SAR constellations. Only altitudes corresponding to valid RGT solutions are shown. Across the sampled RGT altitude range, many configurations provide multiple observation opportunities per day. For example, considering the $\tau = 1/15$ orbit, four interferograms, each with a temporal baseline of one nodal day, could be created assuming acquisitions occur during every opportunity. This would result in a dense interferogram time series with four different pair observation times interspersed throughout a nodal day. The analysis was restricted to RGT orbits with repeat intervals of four days or less because interferometric phase coherence over ice at X-band frequencies typically degrades after 3–4 days, limiting the temporal baseline over which reliable DInSAR measurements can be obtained.

The plot at right in Figure 2 examines the present on-orbit commercial SAR capability by analyzing orbit drift for satellites identified by their North American Aerospace Defense (NORAD) Command catalog identifiers. Drift rates are computed for the period between February 10–17, 2026 to identify spacecraft actively maintaining RGT configurations within the 1–4 day repeat range. Applying a drift threshold reveals three satellites that are consistent with one-day repeat orbits. Independent confirmation from commercial operators, including ICEYE, verifies that these spacecraft are operating in one-day RGTs. This agreement confirms that existing satellites can operationalize dense InSAR time series sampling without changing their orbits.

While the number of observation opportunities is an important metric, further analyses were performed to identify RGT orbits that maximize measurement precision in the context of ice shelf grounding zone dynamics. The design space of one-day RGT orbits in inclination–RAAN coordinates was sampled for measurement precision. Figure 3 presents a tiled set of six figures, all of which plot a measurement precision metric as a function of a given orbit inclination and RAAN. All orbits in the design space were sampled at an altitude of 561 km above a spherical Earth, which is required to satisfy the one-day repeat condition. Colors in each plot indicate the measurement precision for observations of Thwaites Glacier, evaluated using both the geometric Cramér-Rao lower bound (σ_{geo}) and the tidal Cramér-Rao lower bound (σ_{tid}). These performance metrics quantify the achievable measurement precision for secular ice velocity and vertical tidal displacement estimation from the set of observation opportunities in the given orbit. Lower values correspond to improved measurement precision. In the top row of plots, computation of σ_{geo} is only possible when line of sight access to the glacier is present, which occurs for inclination angles within approximately $\pm 17^\circ$ of polar 90°. Within this range, measurement precision exhibits a striped pattern as a function of inclination with decreased precision at low and high inclination angles and increased precision at mid-range inclination angles. Furthermore, strong sensitivity to RAAN is evident for inclinations $\pm 10^\circ$ from 90° where significant gaps appear in the σ_{geo} performance maps.

These data gaps occur due to a requirement of a minimum number of four observations for computation of all of the performance metrics in lieu of the form of the tidal design matrix given in section II-C. While computation of $\sigma_{\text{geo,ver}}$ requires only one observation, a uniform four observation minimum gate was applied to represent the desire for full 3D secular ice velocity estimation and vertical tidal decomposition. The four observation minimum requirement maps to the shared data gaps between the geometric and tidal CRLBs in figure 3. The larger range of data gaps present for the geometric plots is due to insufficient azimuthal diversity in available observation opportunities. Azimuthal ambiguities result in a rank-deficient geometric normal matrix that prevents inversion. On the other hand, poor azimuthal diversity does not produce rank-deficient tidal normal matrices because the tidal design matrix structure is dominated by the temporal sampling pattern. Optimal performance of the geometric and tidal CRLBs occurs in bands of inclination approximately two degrees of latitude south of Thwaites Glacier, where orbital geometry produces the largest number and spatial diversity of line of sight access opportunities. The horizontal and K1 components are observed to dominate the precision of the total geometric and tidal metrics respectively, with $\sigma_{\text{geo,hor}}$ exhibiting larger values than $\sigma_{\text{geo,ver}}$ across nearly the entire design space due to limited azimuthal LOS diversity, and $\sigma_{\text{tid,K1}}$ exceeding $\sigma_{\text{tid,O1}}$ because the K1 frequency lies closer to the nodal day sampling interval and is therefore less well-separated from secular drift than O1. All regions of the worst measurement performance occur along the perimeters of the data gaps due to their proximity to orbit designs with fewer observation opportunities and more azimuthal ambiguity. These results highlight how orbit geometry governs the downstream measurement precision of both three-dimensional ice motion and the tidal forcing signals that drive flexure-zone dynamics and establishes baseline measurement performance capabilities for a single satellite in a one-day RGT orbit.

In addition to the best-performing one-day RGT orbit design extracted from the design space in figure 3, two currently on-orbit SAR systems and a theoretical TWIST InSAR system were considered in a more detailed observation campaign of Thwaites Glacier. Figure 4 shows the geometric and tidal CRLB mapped onto the Thwaites region of interest for each of the SAR systems considered. The figure presents a grid of plots in which columns correspond to distinct observing systems and rows correspond to different CRLB metrics. CRLB metrics were computed for observations spanning four full beat periods between the dominant K1 and O1 diurnal constituents around the Thwaites Glacier region. The spatial distribution of σ_{geo} and σ_{tid} is visualized by overlaying a color map on the region of interest centered on Thwaites Glacier. Eleven markers are shown to indicate the centroids of discrete 30 km $\times$ 50 km target areas corresponding to the standard footprint of a commercial SAR stripmap image [15]. To allow visualization of measurement precision spanning multiple orders of magnitude, the σ_{geo} and σ_{tid} color scales are nonlinear and kept constant across rows.

Across CRLB metrics, the theoretical TWIST InSAR constellation offers the best overall measurement precision, achieving the lowest σ_{geo} and σ_{tid} values across all observa-

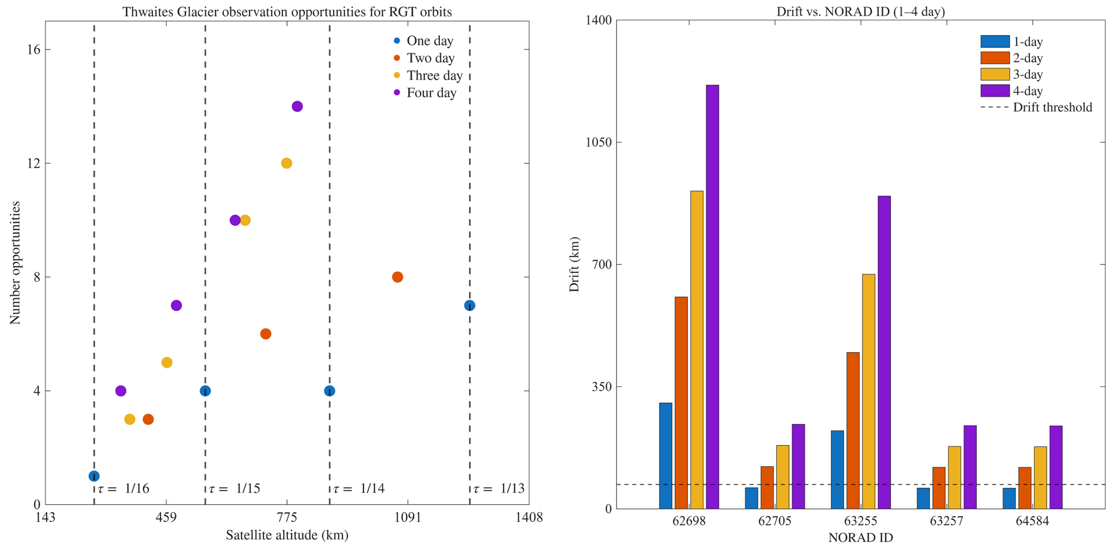

Fig. 2. Left shows the number of observation opportunities of Thwaites Glacier for SAR satellites in repeat ground tracks in low Earth orbit. Four families of repeat ground track orbits with increasing revisit intervals are shown. Similitude parameters are annotated for each of the one-day revisit orbits. Right shows the repeat ground track drift for commercial SAR satellites maintaining altitude between 2/10/2026 and 2/17/2026. Three satellites are identified as having one-day repeat intervals according to a 70 km drift threshold.

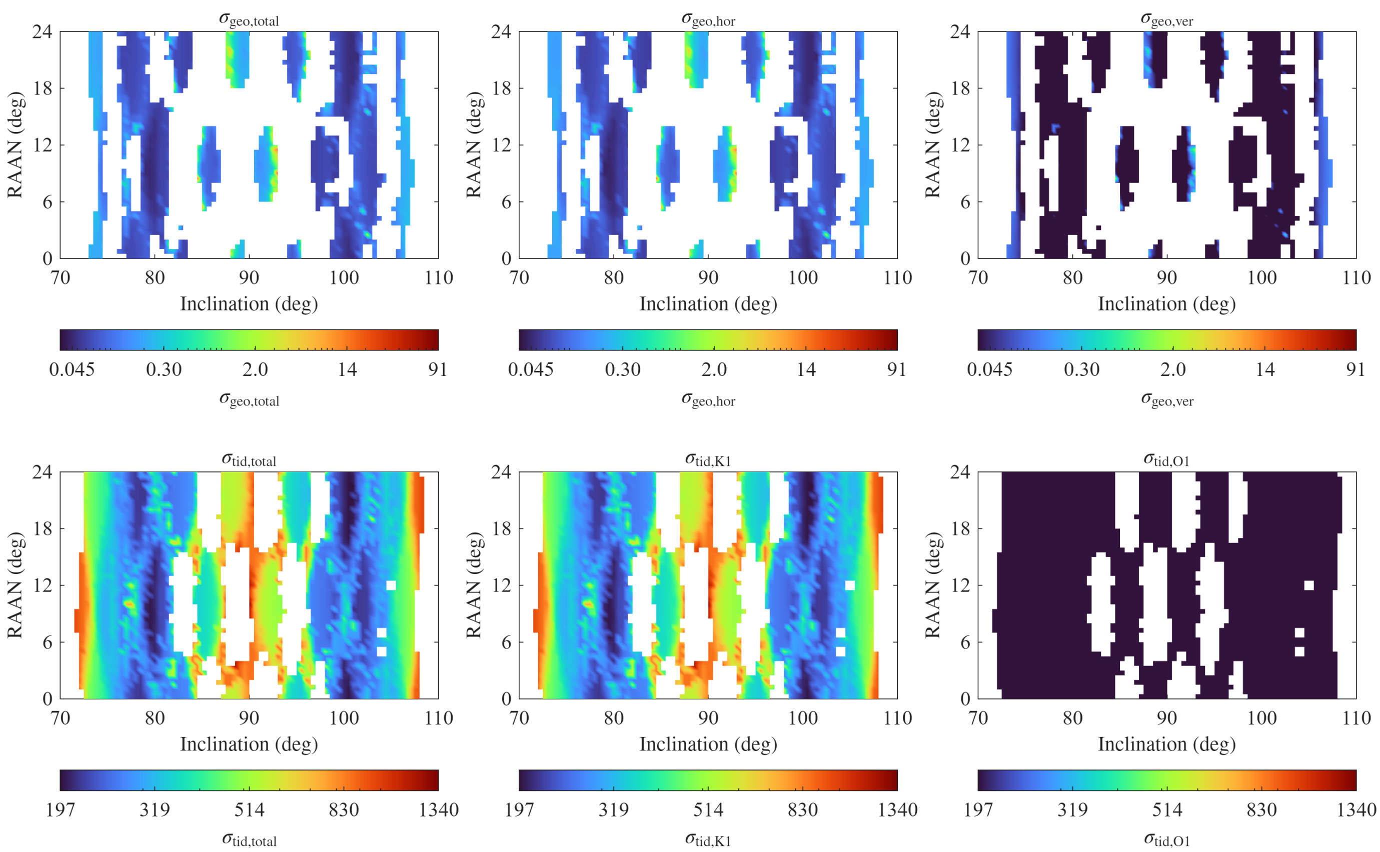

Fig. 3. Average measurement performance of observations of Thwaites Glacier over the one-day repeat ground track design space. Inclination angles covering the entire range of target line of sight access were sampled and the complete range of RAAN for repeat tracks assuming a spherical Earth was sampled. The colormaps for both σ_{geo} and σ_{tid} are logarithmic to visualize gradations in the large range of values.

tion tiles. The geometric and O1 tidal CRLB metrics decrease monotonically across the four columns of figure 4, with each successive observing system yielding a roughly two- to three-fold improvement over the previous. The best performing single satellite one-day RGT orbit and the on-orbit ICEYE three-satellite constellation populate the middle of this trend, with the three-satellite system providing approximately a two-fold reduction in σ_{geo} and $\sigma_{tid,O1}$ over the single-satellite

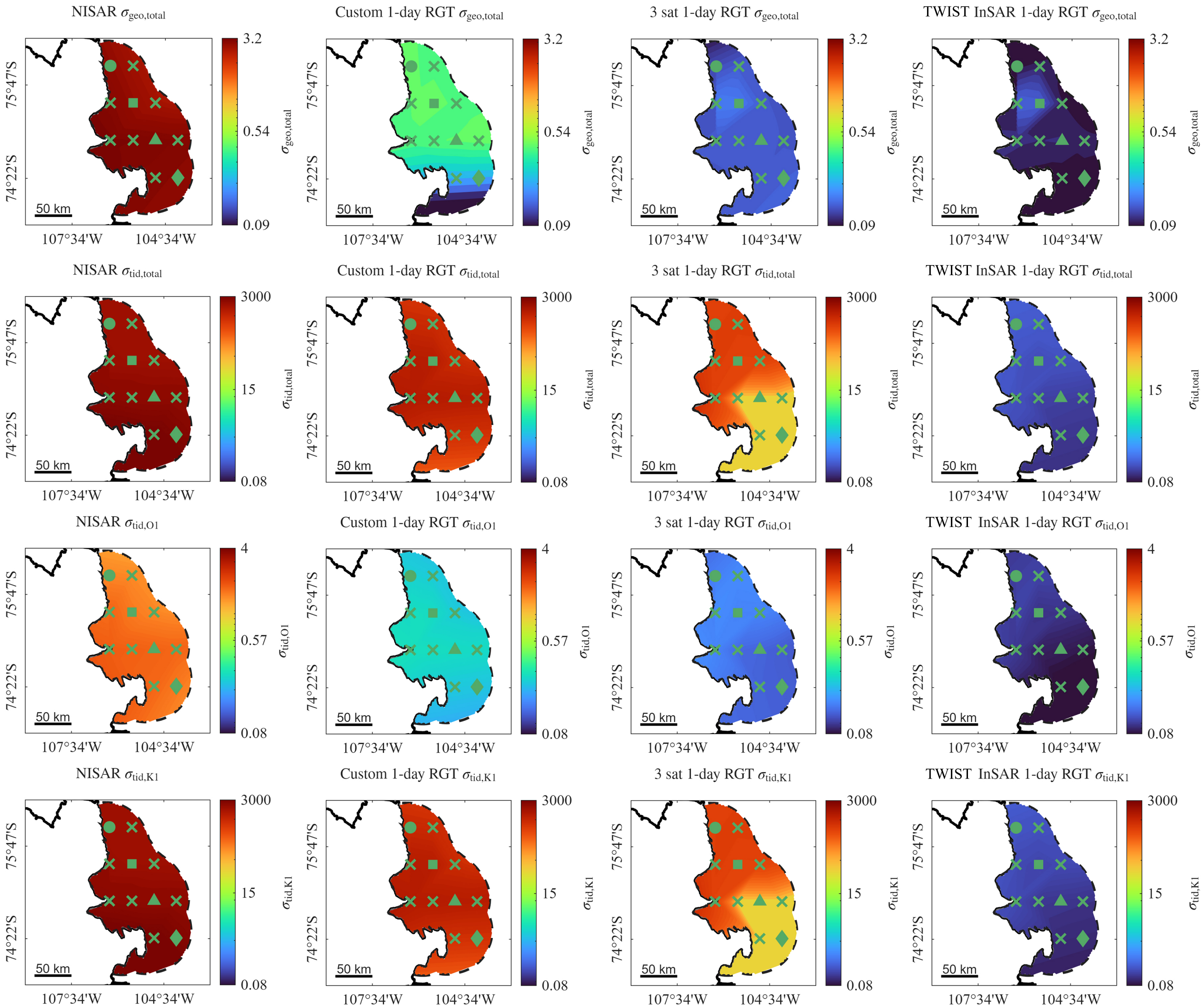

Fig. 4. Spatial distribution of the CRLB fundamental limit of measurement precision for secular ice velocity inversion (top row) and vertical tidal displacement inversion (bottom three rows). Data is plotted for the NISAR satellite (left column), an optimally-designed satellite orbit (middle left column), a currently on-orbit three satellite SAR constellation (middle right column), and a theoretical four satellite SAR constellation (right column). Markers plotted on the region of interest correspond to centroid locations of individual SAR observation tiles. Custom, nonlinear color maps were used to visualize gradations in the large range of values plotted for σ_{geo} and σ_{tid} across observing systems.

case due to the additional geometric diversity and temporal sampling associated with multiple spacecraft. In contrast, the total and K1 tidal CRLBs exhibit a sudden three order-of-magnitude improvement between the ICEYE three-satellite system and the four-satellite TWIST InSAR constellation. This discontinuity reflects the ability of the TWIST InSAR design to break the K1 aliasing problem inherent to one-day RGT sampling. Because the K1 component dominates the total tidal CRLB, the dramatic gain in $\sigma_{tid,K1}$ propagates directly into $\sigma_{tid,total}$, while $\sigma_{tid,O1}$ and the geometric metrics retain their smooth monotonic behavior. Significant spatial variability in CRLB value across the region of interest is also evident for $\sigma_{tid,K1}$ and $\sigma_{tid,total}$, particularly for the ICEYE three-satellite system, whereas σ_{geo} and $\sigma_{tid,O1}$ are spatially homogeneous within each observing system.

Measurement performance for the NISAR satellite consistently under performs relative to the three other observing systems, owing to the limited range of viewing geometries provided by the mission's orbit and repeat cycle. As a monolithic system designed to support a broad portfolio of sensing applications, NISAR's orbit is not optimized for the inversions central to characterizing the stability of Antarctic flexure zones. The best performing single-satellite RGT orbit demonstrates that tailoring orbit design to the inversion of interest yields meaningful gains in measurement precision even with a single spacecraft. However, the strong sensitivity of σ_{geo} and σ_{tid} to both viewing-geometry diversity and temporal sampling density means that constellations of satellites are best suited for this application. Furthermore, precision orbit design, as in the theoretical TWIST InSAR case, delivers two to three order-of-magnitude improvements in the precision of the downstream data products that are critical to informing fundamental understanding of grounding zone dynamics.

Following the continuing proliferation of InSAR-capable SAR satellites on-orbit, the change in measurement precision as a function of the number of on-orbit SAR satellites was quantified. Figure 5 examines how the CRLBs scale for the addition of unphased SAR satellites, each offering InSAR measurements with one-day temporal baselines, and for the addition of phased SAR satellites in TWIST InSAR configurations offering InSAR measurements with sub-daily temporal baselines. The σ_{geo} and σ_{tid} values plotted correspond to the average values across the 11 tiles distributed across the Thwaites Glacier region of interest. Error bars are plotted for each point to indicate the variance in measurement precision across the spatially distributed tiles. The unphased configuration adds satellites to the existing three-satellite constellation with orbital plane RAANs distributed uniformly around the Earth. The phased TWIST InSAR configuration adds each new satellite relative to a reference orbit offering sub-daily temporal baselines across satellites in addition to the one-day temporal baselines present for each individual satellite. Figure 1 in the supplementary material shows histograms of the sub-daily temporal baseline distributions for all constellation sizes. For constellation sizes of one to three satellites, the orbit parameters of the three ICEYE one-day repeat satellites identified in figure 2 are used and both designs are equivalent.

The geometric CRLB exhibits a sudden order-of-magnitude reduction between the one and three satellite cases, after which all components decrease monotonically and the unphased and TWIST configurations yield essentially identical σ_{geo} values across all constellation sizes. As azimuthal diversity increases with additional satellites in unique planes, both $\sigma_{geo,hor}$ and $\sigma_{geo,ver}$ steadily decrease reflecting the improved ability to constrain horizontal and vertical motion from multiple viewing directions. The reductions occur in both the mean values and their variances across the tiles, demonstrating that additional satellites improve not only the value of the CRLB but also the spatial uniformity of precision across the region of interest.

The tidal CRLB exhibits strong contrasts between the two constellation configurations. For the TWIST InSAR configuration, the addition of a single phased satellite to the existing three satellite constellation produces a three order-of-magnitude drop in $\sigma_{tid,K1}$ and $\sigma_{tid,total}$, and the across-tile error bars collapse to near zero. This dramatic improvement reflects the elimination of K1 signal aliasing once sub-daily temporal baselines are introduced, and the performance gradually improves for all subsequent constellation sizes. The unphased InSAR configuration, on the other hand, exhibits a monotonic decrease in $\sigma_{tid,K1}$ and $\sigma_{tid,total}$ and remains three orders of magnitude larger relative to the TWIST InSAR design. The $\sigma_{tid,O1}$ component decreases monotonically for both unphased and phased InSAR configurations because O1 is not aliased by the one-day sampling cadence.

The bottom plot of figure 5 quantifies the increase in the number of feasible interferometric observations and the corresponding reduction in measurement variance as constellation size grows. Each additional satellite in either configuration directly translates into more repeat-pass opportunities, increasing the density of the observation time series. For the three satellite constellation currently operating in one-day RGT orbits, approximately 1,100 feasible InSAR observations of Thwaites Glacier are available over a campaign duration spanning four tidal beat frequencies. After the addition of the first phased satellite, the TWIST InSAR configuration consistently provides more observations and lower measurement variance than the unphased configuration at the same constellation size, owing to the additional sub-daily temporal baseline pairs formed between phased satellites in addition to the daily pairs from each individual satellite. While additional InSAR observations do not bring precipitous improvements in σ_{geo} and σ_{tid} outside of the K1 aliasing threshold, the steady reduction in measurement variance demonstrates added value from larger constellations beyond the precision metrics alone. The presented results quantify measurement precision improvements as a function of observing system size and constellation design configuration, and can serve as evidence for supporting decisions in satellite resource allocation for future observing campaigns of Antarctic flexure zones.

While the previous results enable relative comparisons between observing systems, they do not consider measurement noise or enable direct estimation of deformation within the flexure zone as a function of time due to tidal forcing. To this end, complementary analyses were performed by executing the full inversion for secular motion and vertical tidal displacement as described in [3]. A background velocity field was applied to the Thwaites region of interest using ice surface velocities from the MEaSUREs dataset [13] and the K1 and O1 composite tidal forcing was simulated over four beat periods to produce vertical displacements on the floating portion of the region of interest. For floating ice within a 10 km seaward distance from the grounding line, a vertical displacement dampening function was prescribed following a hyperbolic tangent formulation that decreased from 1 to 0 at the grounding line. Collections of InSAR observations were compiled for each satellite system by propagating over four tidal beat periods. The unit line of sight vectors, line of sight displacements, and observation times, were logged for every feasible InSAR observation and used to formulate the combined secular velocity and vertical tidal displacement design matrix. A data covariance matrix was also defined for every feasible InSAR observation by assigning a pixel-wise coherence value using a Gaussian distribution with mean 0.8 and standard deviation 0.1. Inversions were performed using the design matrices and data covariances and results are shown in figure 6. For completion, a coherence sensitivity analysis was performed and results are presented in figure 2 of the supplementary materials.

All plots in figure 6 correspond to the ice shelf flexure zone, or the 10 km seaward extent of ice from the grounding line of the Thwaites region of interest. Truth curves are shown as solid black lines, inversion estimates are shown as solid blue lines, and the amplitude envelope corresponding to 5th and 95th percentile of pixel amplitudes are shown as light blue shaded regions. Similar to figure 4, columns correspond to different satellite SAR systems. The top three

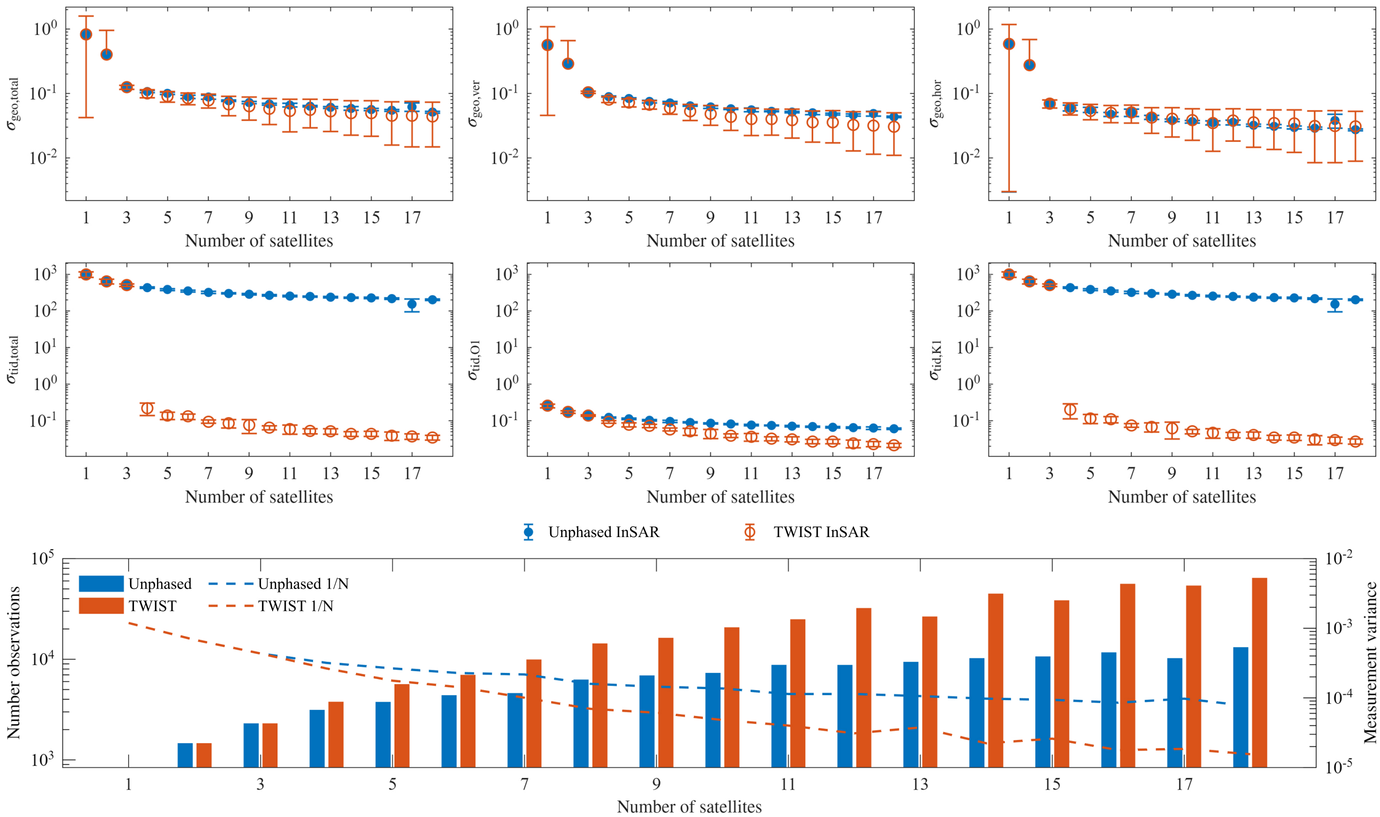

Fig. 5. Measurement precision as a function of number of satellites in a given SAR constellation. Constellations with orbit designs corresponding to single-platform InSAR configuration are plotted in blue while the multi-platform InSAR configuration is plotted in red. The first three satellites correspond to the orbits of the commercial one-day repeat ground track satellites in February 2026. The combined and individual components of σ_{geo} and σ_{tid} are plotted in the first and second rows while the number of InSAR observations and corresponding measurement variance is plotted in the third row.

rows of plots correspond to inverted surface displacement time series for the composite tidal forcing and each of its constituents over a single beat period. The fourth row presents the maximum inverted surface displacement of the ice shelf as a function of distance from the grounding line. Generally, inversion results consistently approach the truth tidal forcing signal when comparing satellite SAR systems from left to right. NISAR's relative infrequency of observations results in a surface displacement time series reconstruction that is dramatically out-of-phase and two orders of magnitude larger in amplitude compared to the true forcing. While the shape of NISAR's maximum inverted surface displacement is in line with expectations, its magnitude is three orders larger than the truth. Surface displacement time series inversions using observations from the best performing one-day RGT satellite estimate O1 tidal amplitudes of the same order as the truth signal. However, the inverted O1 phase estimate is incorrect and a two order of magnitude amplitude error in the K1 estimate is present for this observing system. Furthermore, while the magnitude of the maximum inverted surface displacement is one order of magnitude closer to truth compared to NISAR, the profile as a function of distance from the grounding line remains erroneous. The multi-satellite SAR systems in the right two columns achieve significantly improved inversion performance. The ICEYE three satellite system estimates surface displacement time series with amplitudes of the correct order and phase errors contained within $15°$. The O1 tidal reconstruction is closer to truth in both amplitude and phase compared to the K1 tidal reconstruction. The shape of the maximum inverted surface displacement profile generally follows the truth $\tanh(x)$ form but underestimates amplitude primarily due to underestimation of the K1 tidal amplitude. The inversion performance obtained using observations from the four satellite TWIST InSAR constellation outperforms all other systems. The composite and individual tidal constituent signals are nearly exactly resolved in the surface displacement time series inversions. Additionally, the maximum inverted surface displacement as a function of distance from the grounding line matches the truth profile well and recovers most of the amplitude underestimation present in the inversion using the on-orbit three satellite system.

IV. Discussion

The presented results demonstrate that operationalizing a TWIST InSAR configuration with commercial SAR constellations enables InSAR measurements with sub-daily temporal baselines of Antarctic grounding zones. These observation capabilities represent a substantial improvement over existing DInSAR datasets whose temporal baselines are all integer multiples of a nodal day. The dominant tidal constituents driving flexural deformation near Thwaites Glacier occur at diurnal frequencies, most prominently the K1 and O1 constituents

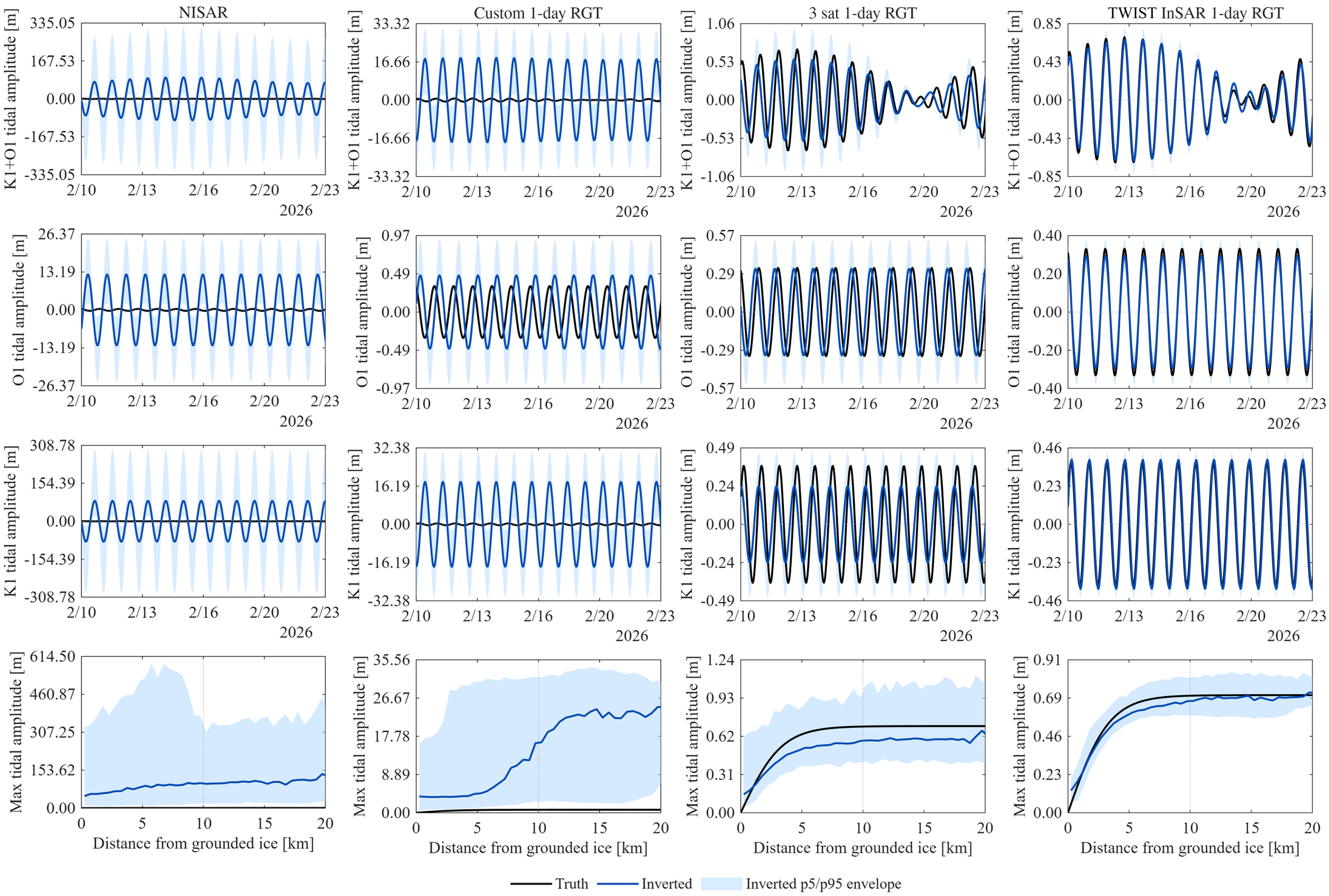

Fig. 6. Inversions of surface displacement of ice shelf grounding zone dynamics from simulated InSAR observations with four different satellite systems. Vertical displacement due to different decompositions of tidal forcing as a function of time is shown in the top three rows. Maximum vertical displacement due to composite tidal forcing as a function of distance from the grounding line is shown in the bottom row. In all cases, inversion fidelity relative to truth increases from left to right indicating that multi-satellite observing systems outperform monolithic systems.

with periods of $T_{\text{K1}} = 23.934$ hr and $T_{\text{O1}} = 25.819$ hr. The density of interferometric pairs progressively increases when comparing the NISAR satellite to the best performing one-day RGT orbit and the ICEYE three-satellite constellation, reducing measurement variance in the ensuing inversions. However, the minimum achievable temporal baseline remains one-day for all of these systems since each observation pair must come from the same satellite revisiting the same RGT position. The corresponding effective sampling frequency for differential measurements is therefore $f_s = 1$ day^{-1}, which lies very close to the K1 forcing frequency $f_{\text{K1}} = 1.0027$ day^{-1} and produces severe aliasing of the K1 signal into long-period drift. TWIST InSAR observations overcome this limitation by acquiring measurements with sub-daily temporal baselines. These temporal baselines are short enough to satisfy the Nyquist criterion for the K1 constituent, breaking the aliasing degeneracy that limits one-day repeat constellations.

TWIST InSAR also enables rapid identification of the phase drift between different tidal constituents. The minimum observation campaign duration required to separate two harmonic signals is governed by the inverse of their frequency difference as shown in equation 6.

$$T_{\text{beat}} = \frac{1}{|f_1 - f_2|} \tag{6}$$

Using the constituent frequencies above, $T_{\text{beat}} = 13.7$ days. The superposition of K1 and O1 produces a modulation cycle of approximately two weeks, and a campaign that spans at least one full beat cycle is sufficient to make the two constituents linearly separable in an inversion for tidal displacement. With approximately nine InSAR pair observation opportunities per day from the four satellite TWIST InSAR constellation, a single beat cycle yields well over one hundred independent measurements, $N_{\text{obs}} \approx 9 \times 13.7 \approx 123$, far exceeding the minimum required to constrain the four cosine and sine coefficients describing the vertical tidal displacement at K1 and O1. This sample density yields a well-conditioned design matrix and a low-variance estimate of the constituent amplitudes, as evidenced by the inverted surface displacement reconstructions in figure 6 that recover the true K1 and O1 signals in both amplitude and phase.

A direct comparison between TWIST InSAR and the one-day temporal baselines that have to this point been the state of the art reveals the magnitude of the benefit. The K1 constituent has a period very close to one nodal day, producing a near-degeneracy when interferometric pairs are formed at exact daily intervals. The apparent alias frequency under daily sampling is $f_{\text{alias}} = |f_{\text{K1}} - 1|$, which yields $T_{\text{alias}} = \frac{1}{|f_{\text{K1}}-1|} = 364$ days. The current state of the art of one-day temporal baseline interferometric pairs therefore requires nearly a full year for the phase difference between the dominant K1 tide and the sampling interval to fully manifest, making it extremely difficult to isolate this constituent. The unphased constellation results in figure 5 demonstrate this difficulty with $\sigma_{\text{tid,K1}}$ remaining stuck near the same value as the three-satellite constellation even as up to 15 additional satellites are added. By contrast, TWIST InSAR pairs with sub-daily temporal baselines immediately resolve the diurnal oscillation and allow the combined K1 – O1 system to be separated over the much shorter 13.7-day beat cycle. This reduction in the required observation duration from on the order of a year to weeks fundamentally changes the feasibility of using satellite InSAR to study the viscoelastic response of ice shelf flexure zones.

Beyond measurement performance, practical satellite operations play an important role in determining whether a sustained observation campaign over Antarctic grounding zones can be maintained. Commercial SAR constellations operate under tasking frameworks designed to balance imaging demand, spacecraft power budgets, and onboard data storage. Typical commercial SAR spacecraft operate with duty cycles of roughly 30% per orbit, reflecting limitations imposed by spacecraft power generation, thermal constraints, and data downlink capacity [32]. Because SAR imaging is one of the most power-intensive spacecraft activities, operators must carefully allocate imaging time within each orbit to ensure sufficient energy margins are maintained. In practice, this requires prioritizing high-value imaging tasks while leaving substantial portions of each orbit available for battery recharging.

These operational considerations are particularly relevant for observations over Antarctica. The demand for commercial imaging requests at polar latitudes is typically much lower than over populated low to mid-latitude regions, meaning that spacecraft time over the Antarctic continent is often used for battery charging and system housekeeping rather than active imaging. As a result, opportunistic acquisitions supporting scientific campaigns can often be scheduled during these otherwise underutilized orbit segments without significant competition with other commercial tasking priorities. In the context of the observation strategies proposed here, this implies that routine interferometric acquisitions over Thwaites Glacier may be achievable without substantially disrupting nominal mission operations.

The constellation analysis presented in this work also highlights the operational advantages of deploying multiple satellites in one-day repeat ground track orbits, an outlook that aligns with the trajectory of the commercial SAR industry. Operators, such as ICEYE, Capella Space, and Umbra Space, have launched new spacecraft every year since 2021, and a growing fraction of these satellites are placed into RGT orbits suitable for interferometric work. While σ_{geo} and σ_{tid} performance exhibit diminishing returns as unphased satellites are added to the existing three satellite constellation, the continued addition of RGT spacecraft is nonetheless essential to the long-term success of the observation campaign proposed here. Distributing imaging opportunities across a larger constellation lowers the duty cycle required of each spacecraft, alleviating power management constraints and reducing conflicts with high-priority commercial imaging requests. From a mission operations perspective, this redundancy increases the robustness of the campaign, as outages, scheduling conflicts, or satellite anomalies are less likely to interrupt the measurement time series when more spacecraft are available to fill in. Newly launched satellites also offer the opportunity to introduce phased orbit planes that produce sub-daily temporal baseline pairs with existing on-orbit assets, transforming what would otherwise be a redundant addition into a TWIST InSAR upgrade that breaks the K1 aliasing barrier.

V. Conclusion

Constraining the stability of Antarctic ice streams and the sea level rise projections that depend on them requires resolving the dynamic response of grounding zone flexure to transient tidal forcing, a signal that has remained largely undocumented due to persistent gaps in the temporal sampling of InSAR measurements. This work addresses that gap through a Cramér-Rao lower bound analysis showing that observation campaigns leveraging currently on-orbit commercial SAR satellites can deliver a two to three-fold improvement in the measurement precision of vertical surface displacement of sensitive regions, such as Thwaites Glacier, over the current state of the art. Furthermore, a TWIST InSAR constellation configuration was shown to deliver a three orders of magnitude improvement by enabling sub-daily temporal baselines that break the K1 tidal aliasing barrier of one-day repeat sampling. The incremental addition of future SAR satellites to the existing constellation was shown to improve both measurement precision and variance through increases in the number of feasible interferometric observations. Full inversions of synthetic surface displacement demonstrated that these precision improvements transfer directly into more faithful recovery of tidal amplitude time series and maximum tidal displacement as a function of distance from the grounding line.

Realization of this improvement in measurement capability is feasible given existing commercial SAR tasking over Antarctica, low commercial imaging demand at polar latitudes, and the constellation redundancy needed to sustain data collection through scheduling conflicts, satellite anomalies, or outages. Fully realizing the multiple orders of magnitude precision gains requires the sub-daily temporal baselines afforded by the TWIST InSAR architecture, which could be explored as part of the upcoming Decadal Survey for Earth Science and Applications from Space through a demonstration mission that leverages existing commercial SAR satellites and introduces a phased orbit plane on a future launch. Such a demonstration would address the transient dynamics of Antarctic flexure zones, a high-priority targeted observable that remains outstanding from prior surveys.

References

[1] C. Schoof, "Ice sheet grounding line dynamics: Steady states, stability, and hysteresis," *Journal of Geophysical Research: Earth Surface*, vol. 112, no. F3, 2007.

[2] S. S. Pegler, "Marine ice sheet dynamics: the impacts of ice-shelf buttressing," *Journal of Fluid Mechanics*, vol. 857, pp. 605–647, 2018.

[3] B. Minchew, M. Simons, B. Riel, and P. Milillo, "Tidally induced variations in vertical and horizontal motion on rutford ice stream, west antarctica, inferred from remotely sensed observations," *Journal of Geophysical Research: Earth Surface*, vol. 122, no. 1, pp. 167–190, 2017.

[4] J. Mouginot, E. Rignot, and B. Scheuchl, "Sustained increase in ice discharge from the amundsen sea embayment, west antarctica, from 1973 to 2013," *Geophysical Research Letters*, vol. 41, no. 5, pp. 1576–1584, 2014.

[5] C. R. Williams, R. C. Hindmarsh, and R. J. Arthern, "Frequency response of ice streams," *Proceedings of the Royal Society A: Mathematical, Physical and Engineering Sciences*, vol. 468, no. 2147, pp. 3285–3310, 2012.

[6] P. Milillo, E. Rignot, P. Rizzoli, B. Scheuchl, J. Mouginot, J. Bueso-Bello, and P. Prats-Iraola, "Heterogeneous retreat and ice melt of thwaites glacier, west antarctica," *Science Advances*, vol. 5, no. 1, p. eaau3433, 2019.

[7] E. Rignot, E. Ciracì, B. Scheuchl, V. Tolpekin, M. Wollersheim, and C. Dow, "Widespread seawater intrusions beneath the grounded ice of thwaites glacier, west antarctica," *Proceedings of the National Academy of Sciences*, vol. 121, no. 22, p. e2404766121, 2024.

[8] A. A. Robel, C. Schoof, and E. Tziperman, "Persistence and variability of ice-stream grounding lines on retrograde bed slopes," *The Cryosphere*, vol. 10, no. 4, pp. 1883–1896, 2016.

[9] S. H. Rosier, R. Reese, J. F. Donges, J. De Rydt, G. H. Gudmundsson, and R. Winkelmann, "The tipping points and early warning indicators for pine island glacier, west antarctica," *The Cryosphere*, vol. 15, no. 3, pp. 1501–1516, 2021.

[10] E. Rignot, B. Scheuchl, J. B. Barre, V. Brancato, L. Charrier, H. Chen, E. Ciraci, A. Dinh, S. Herreid, S. Jeong *et al.*, "Thirty years of glacier grounding line retreat in antarctica," *Proceedings of the National Academy of Sciences*, vol. 123, no. 10, p. e2524380123, 2026.

[11] E. L. Kramer and B. M. Minchew, "Space-based insar with sub-daily temporal baselines," 2026, preprint. [Online]. Available: https://eartharxiv.org

[12] C. A. Greene, D. E. Gwyther, and D. D. Blankenship, "Antarctic mapping tools for matlab," *Computers & Geosciences*, vol. 104, pp. 151–157, 2017.

[13] J. Mouginot, B. Scheuchl, and E. Rignot, "Measures antarctic boundaries for ipy 2007-2009 from satellite radar, version 2," 2017. [Online]. Available: http://nsidc.org/data/NSIDC-0709/versions/2

[14] E. Rignot, S. Jacobs, J. Mouginot, and B. Scheuchl, "Ice-shelf melting around antarctica," *Science*, vol. 341, no. 6143, pp. 266–270, 2013.

[15] V. Ignatenko, P. Laurila, A. Radius, L. Lamentowski, O. Antropov, and D. Muff, "Iceye microsatellite sar constellation status update: Evaluation of first commercial imaging modes," in *IGARSS 2020-2020 IEEE International Geoscience and Remote Sensing Symposium*. IEEE, 2020, pp. 3581–3584.

[16] G. Farquharson, D. Castelletti, S. De, C. Stringham, N. Yague, V. C. Bes, J. Ryu, and Y. Goncharenko, "The new capella space satellite generation: Acadia," in *IGARSS 2023-2023 IEEE International Geoscience and Remote Sensing Symposium*. IEEE, 2023, pp. 1513–1516.

[17] S. L. Howard, S. Erofeeva, and L. Padman, "Cats2008: Circum-antarctic tidal simulation version 2008," 2019. [Online]. Available: https://doi.org/10.15784/601235

[18] S. D. Vtipil and B. Newman, "Determining an earth observation repeat ground track orbit for an optimization methodology," *Journal of Spacecraft and Rockets*, vol. 49, no. 1, pp. 157–164, 2012.

[19] D. Mortari, M. P. Wilkins, and C. Bruccoleri, "The flower constellations," *The Journal of the Astronautical Sciences*, vol. 52, no. 1, pp. 107–127, 2004.

[20] M. Zink, A. Moreira, I. Hajnsek, P. Rizzoli, M. Bachmann, R. Kahle, T. Fritz, M. Huber, G. Krieger, M. Lachaise *et al.*, "Tandem-x: 10 years of formation flying bistatic sar interferometry," *IEEE Journal of Selected Topics in Applied Earth Observations and Remote Sensing*, vol. 14, pp. 3546–3565, 2021.

[21] A. A. Thompson*, "Overview of the radarsat constellation mission," *Canadian Journal of Remote Sensing*, vol. 41, no. 5, pp. 401–407, 2015.

[22] M. Virelli, A. Coletta, and M. L. Battagliere, "Asi cosmo-skymed: Mission overview and data exploitation," *IEEE Geoscience and Remote Sensing Magazine*, vol. 2, no. 2, pp. 64–66, 2014.

[23] T. Yamamoto, Y. Arikawa, Y. Ueda, H. Itoh, Y. Nishida, S. Ukawa, H. Tsuru, and M. Yamamoto, "Autonomous precision orbit control considering observation planning: Alos-2 flight results," *Journal of guidance, control, and dynamics*, vol. 39, no. 6, pp. 1244–1264, 2016.

[24] Y. Roa, P. Rosell, A. Solarte, L. Euillades, F. Carballo, S. García, and P. Euillades, "First assessment of the interferometric capabilities of saocom-1a: New results over the domuyo volcano, neuquén argentina," *Journal of South American Earth Sciences*, vol. 106, p. 102882, 2021.

[25] K. Kellogg, P. Hoffman, S. Standley, S. Shaffer, P. Rosen, W. Edelstein, C. Dunn, C. Baker, P. Barela, Y. Shen *et al.*, "Nasa-isro synthetic aperture radar (nisar) mission," in *2020 IEEE aerospace conference*. IEEE, 2020, pp. 1–21.

[26] D. Vallado, P. Crawford, R. Hujsak, and T. S. Kelso, "Revisiting spacetrack report# 3," in *AIAA/AAS astrodynamics specialist conference and exhibit*, 2006, p. 6753.

[27] T. Kelecy, D. Hall, K. Hamada, and D. Stocker, "Satellite maneuver detection using two-line element (tle) data," in *Proceedings of the Advanced Maui Optical and Space Surveillance Technologies Conference*. Maui Economic Development Board (MEDB) Maui, HA, 2007, pp. 1–10.

[28] S. Lemmens and H. Krag, "Two-line-elements-based maneuver detection methods for satellites in low earth orbit," *Journal of Guidance, Control, and Dynamics*, vol. 37, no. 3, pp. 860–868, 2014.

[29] B. Minchew, M. Simons, S. Hensley, H. Björnsson, and F. Pálsson, "Early melt season velocity fields of langjökull and hofsjökull, central iceland," *Journal of Glaciology*, vol. 61, no. 226, pp. 253–266, 2015.

[30] A. M. Stuart, "Inverse problems: a bayesian perspective," *Acta numerica*, vol. 19, pp. 451–559, 2010.

[31] A. Tarantola, *Inverse problem theory and methods for model parameter estimation*. SIAM, 2005.

[32] W. S. Shambaugh, "Doing battle with the sun: Lessons from leo and operating a satellite constellation in the elevated atmospheric drag environment of solar cycle 25," in *Small satellites systems and services symposium (4S 2024)*, vol. 13546. SPIE, 2025, pp. 52–71.

Evan L. Kramer is the Director's Postdoctoral Fellow in the Seismological Laboratory within the Caltech Geological and Planetary Sciences division. He received a PhD and SM in aeronautics and astronautics from MIT in 2025 and 2022 and a BS in aerospace engineering from the University of Maryland, College Park in 2020. Evan's research interests lie in remote sensing system design, science-aware observation planning, and data processing algorithm development.

Brent M. Minchew is a Professor of Geophysics in the Seismological Laboratory within the Caltech Geological and Planetary Sciences division. He received a PhD in geophysics from Caltech in 2016 and a MS and BS in aerospace engineering from UT Austin in 2010 and 2008. Brent's research interests lie in studying the mechanics of glacier beds, ice rheology, and ice-ocean interactions using satellite radar, mathematical theory, and machine learning to constrain near-term rates of sea level rise.

Supplemental material: Magnitude-order improvements to the measurement precision of Antarctic grounding zone dynamics using SAR satellite constellations

Evan L. Kramer, and Brent M. Minchew,

Multi-platform InSAR orbit design

Figure 1 presents the distribution of interferometric temporal baselines for SAR constellations of increasing size. Each panel is a histogram of the number of feasible InSAR observation pairs, N_{pairs}, as a function of temporal baseline measured in sidereal days, with the constellation size, N_{const}, indicated in each panel title. The first three panels correspond to constellations built from one to three of the existing on-orbit SAR satellites referenced throughout the main text. These satellites operate in uncoordinated one-day repeat ground track orbits and therefore only form interferometric pairs at integer nodal day baselines. In accordance, the histograms show discrete spikes at exactly 1, 2, 3, and 4 nodal days for constellation sizes up to 3. Increasing the constellation size from one to three satellites raises the number of pairs available at each integer baseline but does not introduce any fractional baseline values, reflecting the fundamental one-day sampling limitation inherent to the on-orbit constellation.

Satellites added beyond the three-satellite constellation correspond to theoretical future deployments in a TWIST InSAR configuration relative to an existing template satellite. The TWIST InSAR configuration unlocks interferometric pairs at non-integer nodal day baselines, first appearing in the $N_{const} = 4$ panel. The first phased satellite is configured to sample Thwaites at one-quarter of a nodal day relative to the template, while constellations containing more than one phased satellite use equally spaced nodal day offsets. As additional phased satellites are introduced, the histograms progressively fill in the gaps between integer baselines, expanding the coverage of sub-daily temporal baselines until, for the largest constellations, the distribution becomes nearly continuous across the full zero to four day range. This expanding baseline coverage is the mechanism by which TWIST InSAR constellations break the one-day sampling barrier and enable elucidation of the diurnal tidal constituents discussed in the main text.

Inversion robustness to varying coherence

Figure 2 demonstrates the robustness of the inversion results to variations in the data covariance matrix, which is governed by measurement noise dominated by interferometric phase coherence. The figure presents inversion residuals for the four observing systems considered in this work, with columns corresponding to the distinct observing systems and rows corresponding to different residual quantities. The top three rows show the residual of the composite K1–O1 vertical displacement and the residuals of the individual O1 and K1 vertical displacement constituents as a function of time, while the bottom row shows the residual of the maximum vertical displacement as a function of distance along the flexure zone profile. Within each panel, three curves are plotted corresponding to the three mean coherence values identified in the legend, $\bar{\gamma} = 0.1$, 0.5, and 0.9, which set the magnitude of the synthetic measurement noise applied to the line of sight displacements.

Across all observing systems and all residual quantities, the inversion residuals are largely invariant with respect to the assigned mean coherence value, with the three curves remaining closely overlapped in every panel. This insensitivity indicates that the number of InSAR observations accumulated over the four beat period propagation window is sufficient to recover consistent vertical displacement estimates regardless of the noise present in any individual line of sight displacement measurement. The result holds even for the NISAR configuration, which has the sparsest sampling of the four systems. These findings provide confidence that a robust data collection campaign can reliably estimate ice shelf tidal responses despite the various sources of measurement noise, including low phase coherence, encountered in real-world InSAR observations.

E. Kramer and B. Minchew are with the Division of Geological and Planetary Sciences, California Institute of Technology, Pasadena, CA, 91125 USA e-mail: elkramer@caltech.edu

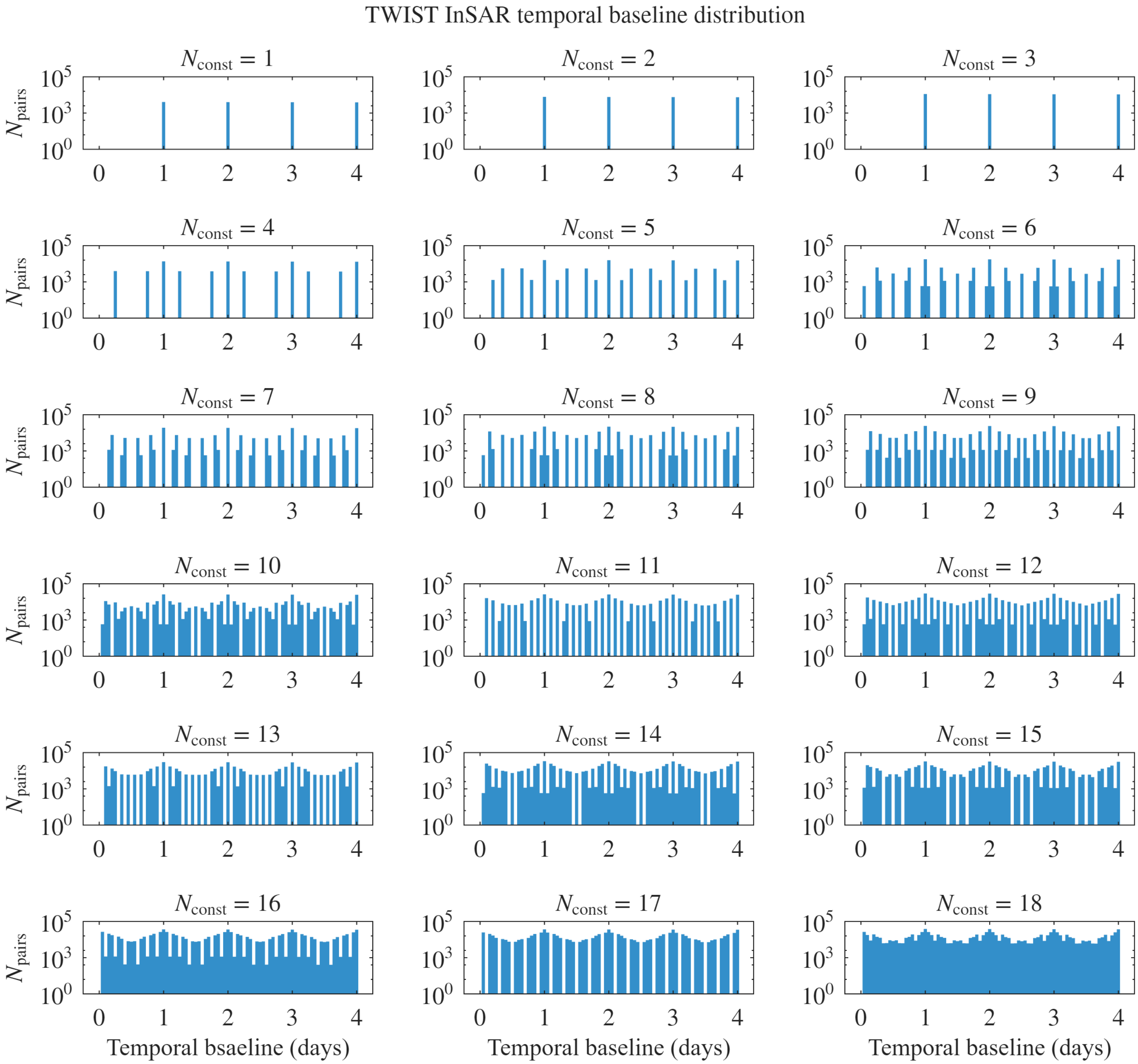

Fig. 1. Temporal baseline distributions for InSAR observations of Thwaites Glacier from SAR constellations of increasing size. The first three satellites correspond to currently on-orbit commercial SAR satellites. Each additional satellite to the existing three are in a TWIST InSAR configuration and offer sub-daily temporal baseline InSAR measurements of Thwaites Glacier.

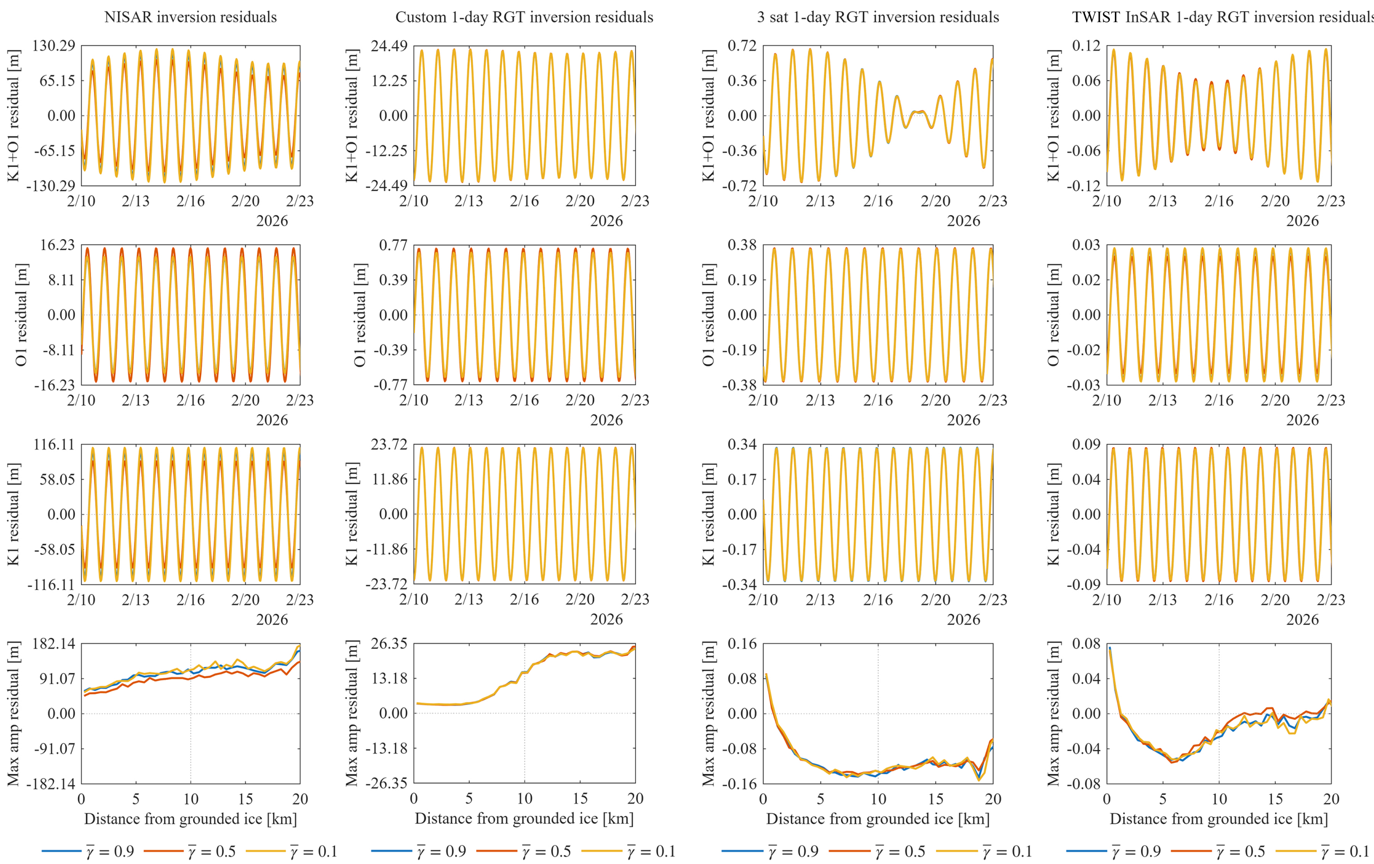

Fig. 2. Vertical displacement inversion time series residuals for varying mean coherence values. The number of InSAR observations across all satellite systems is sufficient for consistent inversion convergence.